Ultrasonics 94 (2019) 292–304

Contents lists available at ScienceDirect

Ultrasonics

journal homepage: www.elsevier.com/locate/ultras

A novel method of reducing the acoustic emission wave reflected by boundary based on acoustic black hole

Xiaoran Wang, Xiandong Liu, Junfei Tai, Tian He*, Yingchun Shan

School of Transportation Science and Engineering, Beihang University, Beijing 100191, China

ARTICLE INFO

Keywords:
Acoustic emission
Boundary reflection
Acoustic black hole
Orthogonal test
Finite element

ABSTRACT

Due to the difference between the characteristic impedance of air and plate structure, the acoustic emission (AE) wave propagating in a plate structure is reflected when reaching the boundary. It leads to the fact that the obtained signal contains not only direct AE components but also reflected components. The existence of the reflected AE wave brings error and difficulty to accurate AE source analysis. This paper attempts to introduce the acoustic black hole (ABH) into an experimental plate structure (a disc structure in this paper) to attenuate the reflected AE wave from the structure boundary and obtain the high Signal-Noise Ratio (SNR) direct AE wave. Firstly, the finite element model of a disc with an ABH is established to verify the attenuation of the reflected AE wave. Then, the orthogonal test is conducted to reveal the influence of geometric parameters of the ABH on reflection attenuation. And a method based on the optimal parameter combination of the ABH is proposed to attenuate boundary reflection. Finally, the broken-lead and friction experiments are performed on the processed disc with the ABH to verify the ability of the ABH to attenuate the boundary reflection of AE wave. Both analytical and experimental results show that the ABH is a candidate tool to reduce the reflected AE wave on the boundary.

1. Introduction

The acoustic emission (AE) experiments are often performed on the plate-like structures [1–4], such as friction experiments, structure damage localization, etc. Due to the large difference of characteristic impedance between the air and the solid plate structure, the reflection of AE wave takes place when the AE wave reaches the boundary. It leads to the fact that the obtained AE signals often contain obvious reflection components. In addition, the frequency dispersion and waveform conversion of the reflected signals during the propagation process may also interfere the characteristic information of the signal source. It makes the feature extraction and the experimental analysis become more difficult. For example, when the friction characteristics are studied by using AE, the AE signal caused by friction propagates in all directions of the structures, and reacts with the subsequent AE signals, increasing the difficulty to reveal the friction mechanism [1]. In this paper, the frictional AE experiment is taken as an example to study the method of reducing the reflected AE wave at the boundary.

It is well known that friction is a complex phenomenon influenced by a variety of factors [5–8]. Despite a number of investigations are carried out on the dynamics of friction, there are still many unanswered questions. For example, the transition between static and dynamic frictions in a contact pair is still unclear. One general way to investigate the transition process is AE technique (AET). One outstanding characteristics of this method presently available is that both the recording of elastic waves and the monitoring of the AE's continuous activity may be performed in real time. Some researchers studied the mechanisms of friction, particularly the transition from stick to slip, via the AE waves which are radiated from the frictional interface in the same way by which the seismologists studied the faulting via seismic waves. The goal of this research is to distinguish different types or modes of rupture which may occur during the transition from stick to slip [9,10].

One of the main problems that arise when studying this phenomenon is the wave arrival is much more difficult to be identified because the 0–200 μs separation between the first main arrival and the second main arrival is not enough for the waves in the plate to be obviously damped due to the material damping (internal friction). For example, in the experiment of localizing the structure damage, the obtained signal contains not only the direct AE wave but also the reflected one. The existence of the reflected AE wave brings error and difficulty to accurate AE source analysis [11,12]. Therefore, some measures were taken in advance to reduce the reflected signals during the AE experiment. Chen [13,14] denoised AE signals that contain electromagnetic impulse noise. Zvokelj [15] proposed a new noise reduction method based on

* Corresponding author.
E-mail address: hetian@buaa.edu.cn (T. He).

https://doi.org/10.1016/j.ultras.2018.08.015
Received 2 July 2018; Received in revised form 16 August 2018; Accepted 16 August 2018
Available online 18 August 2018
0041-624X/

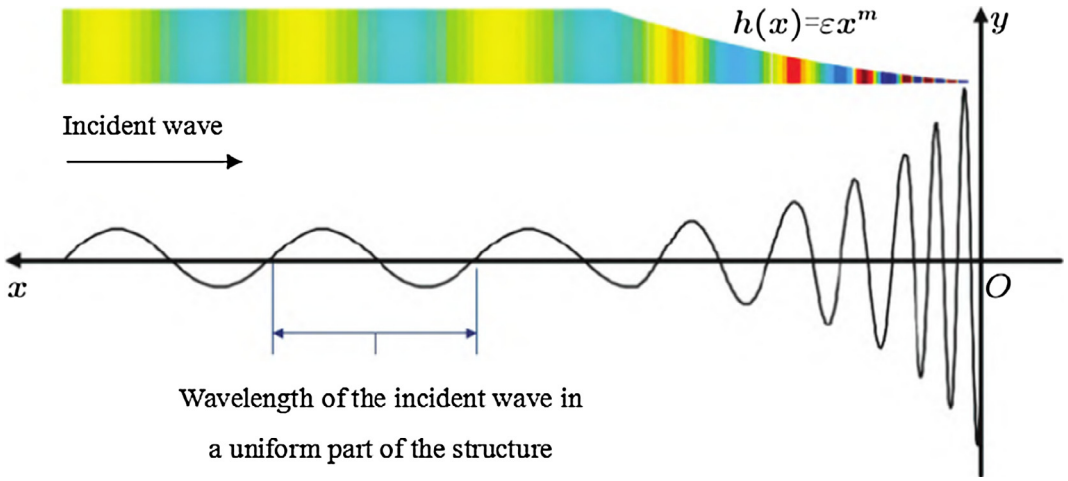

Fig. 1. Propagation of flexural wave in the one-dimensional ABH.

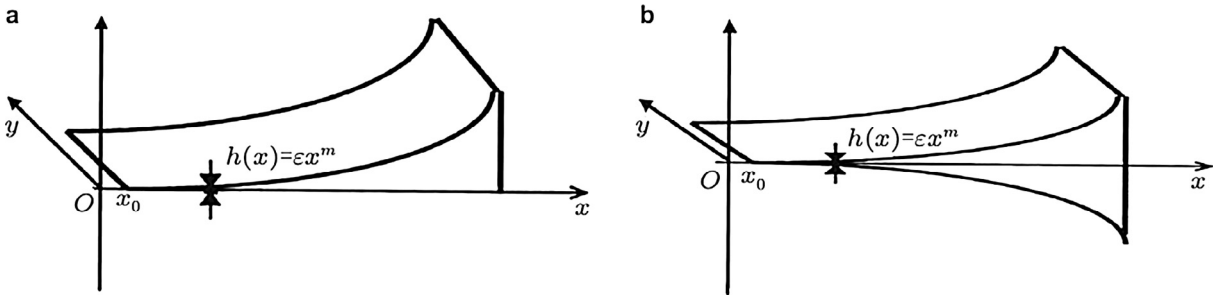

Fig. 2. Wedge edge of a typical one-dimensional acoustic black hole structure.

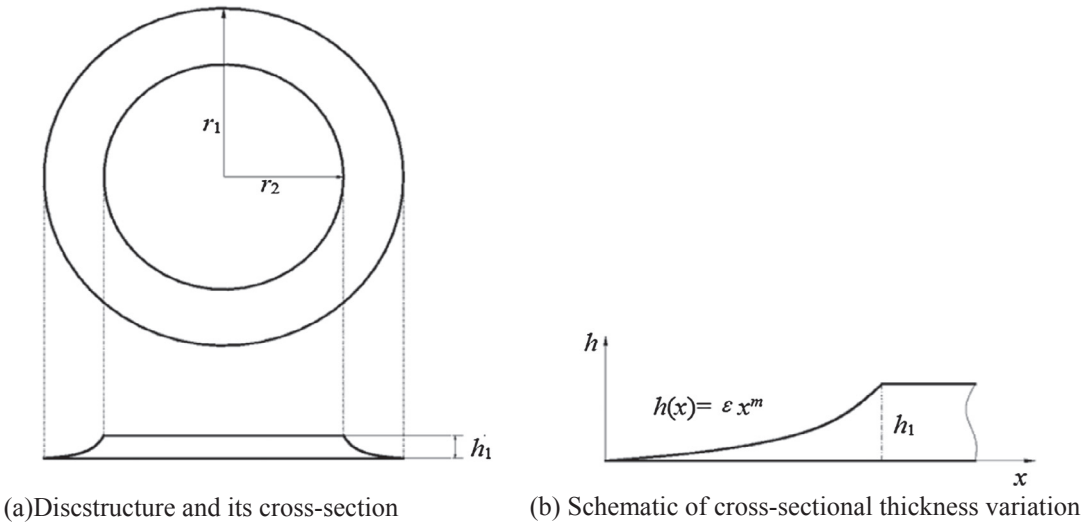

Fig. 3. Disc structure with one-dimensional acoustic black holes.

empirical mode decomposition for noise reduction of AE signals. In addition, some scholars proposed the denoising methods for AE signal based on Empirical Mode Decomposition (EMD) [16], Hilbert-Huang Transform (HHT) [17], and particle filter techniques [18], which can be used for complex non-stationary signal analysis. However, it can be seen that all these methods are only useful to reduce the noise signals in the obtained signals. Actually, in some cases with strong disturbing signals, the key features of weak signals cannot be figured out though these methods are performed deliberately. Since the reflected signal of AE wave produced by the boundary is a great disturbing signal, the obtained signal will be purer and the signal-to-noise ratio will be increased if the reflected signal is reduced before reaching sensor. Then the detection accuracy will be improved. Fortunately, an approach called 'acoustic black hole (ABH)' theory has attracted some attention in the literature [19–24] and is potential for the purpose.

Applications of ABH for flexural waves in plates were introduced and investigated during the last decade. It was first discussed by Mironov who showed that if the thickness of a plate structure decreases smoothly to zero towards its edge, the speed of the flexural waves slows down and approaches zero at the edge. It means that the wave would

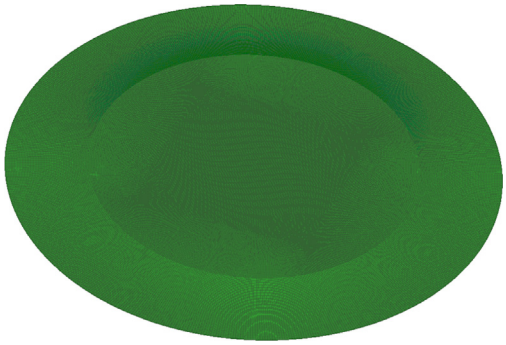

Fig. 4. Disc structure finite element model with one-dimensional acoustic black hole.

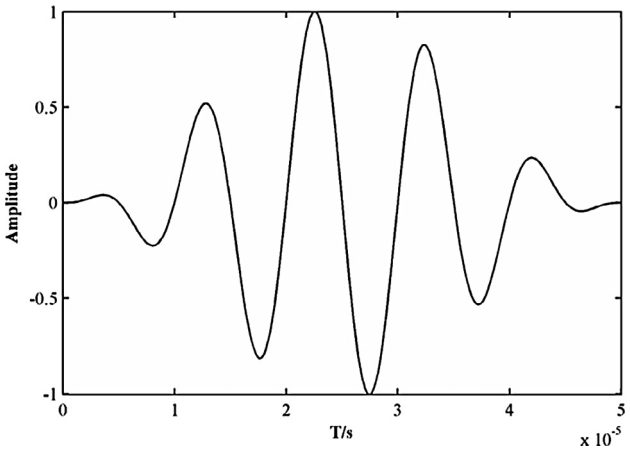

Fig. 5. Five-cycle burst tone excitation at 0.1 MHz frequency.

Table 1
Material properties and geometrical parameters.

Parameters	E	ρ	ν	m	h_1
Value	209	7800	0.3	2.2	5
Units	GPa	Kg/m^3	/	/	mm

never reach the edge, thus no reflection occurs [25]. This phenomenon is referred to as the ABH effect.

This paper attempts to introduce the ABH to a disc to attenuate the reflection AE wave from the structure boundary before reaching the sensor. The organization of this paper is as follows. Boundary anti-reflection method based on the ABH theory is presented in Section 2. In Section 3, the orthogonal test is conducted to reveal the influence of geometric parameters of the ABH on reflection attenuation. And a method based on the optimal parameter combination of the ABH is proposed to attenuate boundary reflection. The ability of the ABH to attenuate the boundary reflection of AE wave is verified by the experiment in Section 4. Finally, the conclusions are drawn in Section 5.

2. Boundary anti-reflection method based on the acoustic black hole theory

2.1. Acoustic black hole theory

As shown in Fig. 1, the one-dimensional acoustic black hole structure satisfies a thickness profile following the power law equation as $h(x) = \varepsilon x^m (m \geqslant 2)$ [26]. When the taper power m is equal to or greater than 2 and the decreasing rate of thickness is sufficiently slow, incident flexural waves are theoretically expected to travel infinite amount of time to reach the tip of the ABH, implying perfect absorption [22].

Fig. 2(a) and (b) show the wedge edges of an ABH with asymmetric and symmetrical cross section, respectively. The governing equation for the movement of a flexural wave in the wedge structure is given by [27]

$$\frac{\partial^2}{\partial x^2}\left[D(x)\left(\frac{\partial^2 w}{\partial x^2}+\nu\frac{\partial^2 w}{\partial y^2}\right)\right]+2(1-\nu)\frac{\partial^2}{\partial x\partial y}\left[D(x)\left(\frac{\partial^2 w}{\partial x\partial y}\right)\right]+\frac{\partial^2}{\partial y^2}\left[D(x)\left(\frac{\partial^2 w}{\partial y^2}+\nu\frac{\partial^2 w}{\partial x^2}\right)\right]-\omega^2\rho h(x)w=0 \tag{1}$$

where the variables w and ρ denote deflection and density respectively. $D(x) = Eh^3(x)/12(1-\nu^2)$ represents bending rigidity. ν and E are Poisson's ratio and Young's modulus, respectively.

When the geometric acoustic approximation method [28,29] is used to solve the motion control equation of the flexural wave in the wedge structure, it is assumed that the lateral displacement $w(x)$ at the position corresponding to the structure can be expressed by following plural form

$$w(x) = A(x)e^{i\Phi(x)} \tag{2}$$

where $A(x)$ and $\Phi(x) = \kappa_p\phi(x, y)$ are the change amplitude and the accumulated phase, respectively. κ_p is the wave number of the uniform part in the plate. $\phi(x, y)$ is eikonal equation.

Substituting Eq. (2) into Eq. (1), both of the real and imaginary parts on the left of the equation must be zero to make the equation true. Letting the real part be zero and omitting the high-order derivative terms for $A(x)$ and $\Phi(x)$, the $\kappa(x)$ can be written by

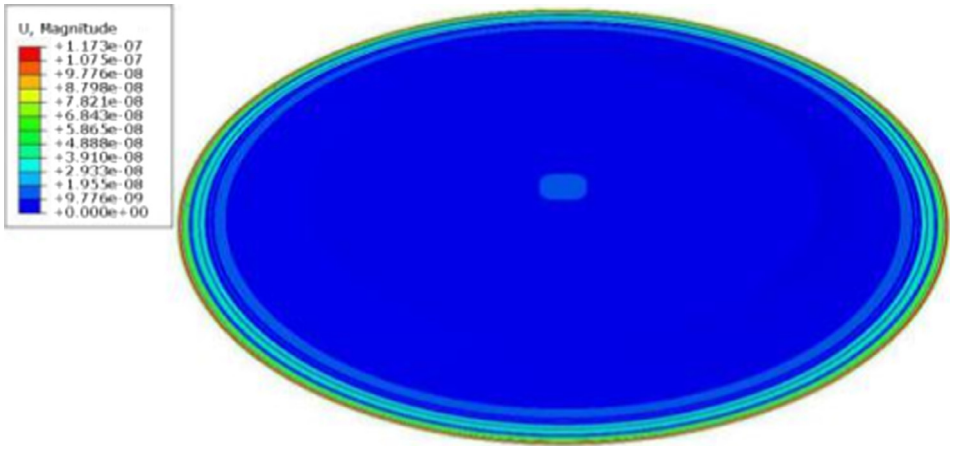

Fig. 6. Displacement cloud of the disc with acoustic black hole.

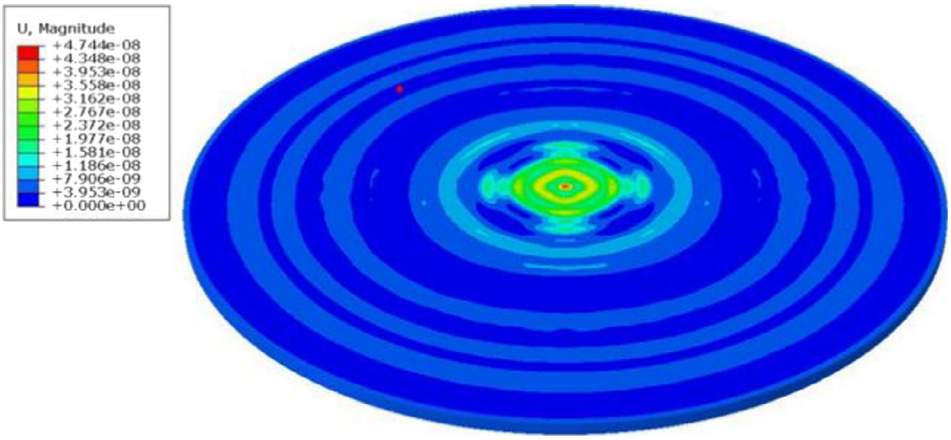

Fig. 7. Displacement cloud of the disc without acoustic black hole.

Table 2
Factors and levels.

Levels	Factors		
	(a) Non-uniform thickness edge length a (mm)	(b) Distance of the sensor from the edge of the upper surface b (mm)	(c) Radius of the upper surface of the disc r_2 (mm)
1	30	20	100
2	40	40	150
3	50	60	200

Table 3
Orthogonal test table.

Test number	Factors			
	(a)	(b)	(c)	Empty column
(1)	1	1	1	1
(2)	1	2	2	2
(3)	1	3	3	3
(4)	2	1	2	3
(5)	2	2	3	1
(6)	2	3	1	2
(7)	3	1	3	2
(8)	3	2	1	3
(9)	3	3	2	1

$$\kappa(x) = \left(\frac{12\kappa_p^2}{(\varepsilon x^m)^2}\right)^{1/4} \tag{3}$$

where $\kappa(x)$ is a position related wave number.

The cumulative phase $\Phi(x)$ can also be written as the integral expression from any point of the wedge to the wedge edge

$$\Phi = \int_0^x \kappa(x)dx \tag{4}$$

From Eqs. (3) and (4), we can get that when $m \geqslant 2$, Φ tends to infinity. It means the flexural waves will not reach the edge. Therefore, it never reflects back either. It is so called the “acoustic black hole” effect.

2.2. Boundary anti-reflection method based on the acoustic black hole theory

2.2.1. Disc model

The experiments based on AE are often performed on the plate structures. In order to eliminate the influence of four sharp corners of the plate structure, the experimental plate can be processed into a disc to better reduce the reflection of the boundary. The disc with the ABH studied in this paper is a one-dimensional ABH structure, which is shown in Fig. 3.

The radius of the equal thickness part is r_2 and the thickness is h_1; The length of the edge thickness change part (the ABH part) is $a = r_1 - r_2$. The thickness changes by a power function $h(x) = \varepsilon x^m$ $(0 \leqslant x \leqslant a,\ m \geqslant 2)$. When $x = a$, $h(a) = \varepsilon a^m = h_1$.

2.2.2. Simulation analysis

This work uses the commercial software Abaqus/Explicit. The theoretical background of the finite element method (FEM) is presented briefly prior to the detailed description on the established FE model. For further understanding, the readers may refer to the literatures [30] and [31]. The Abaqus/Explicit algorithm is computationally efficient for the analysis of large models with relatively short dynamic response times, which makes it optimal for high frequency simulations. Explicit schemes, as used in Abaqus/Explicit, obtain values for dynamic quantities at $t + \Delta t$ based entirely on available values at time t. In this section two fundamental finite element criteria are described, which influence the accuracy and efficiency of a simulation.

(1) Integration time step

The default setting of Abaqus/Explicit is to calculate this time step by

$$\Delta t \approx \frac{l_{e\min}}{c_L} \tag{5}$$

where $l_{e\min}$ is the smallest element dimension in the mesh and c_L is the wave speed of longitudinal waves.

A general rule [32] to describe the relation of the time increment Δt and the maximal frequency of interest $f_{\max}$ is

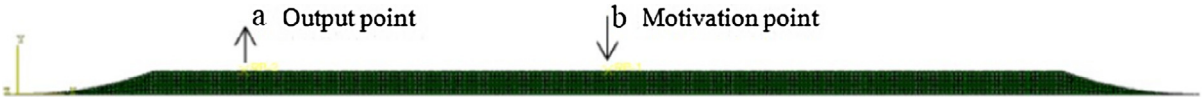

Fig. 8. The finite element model.

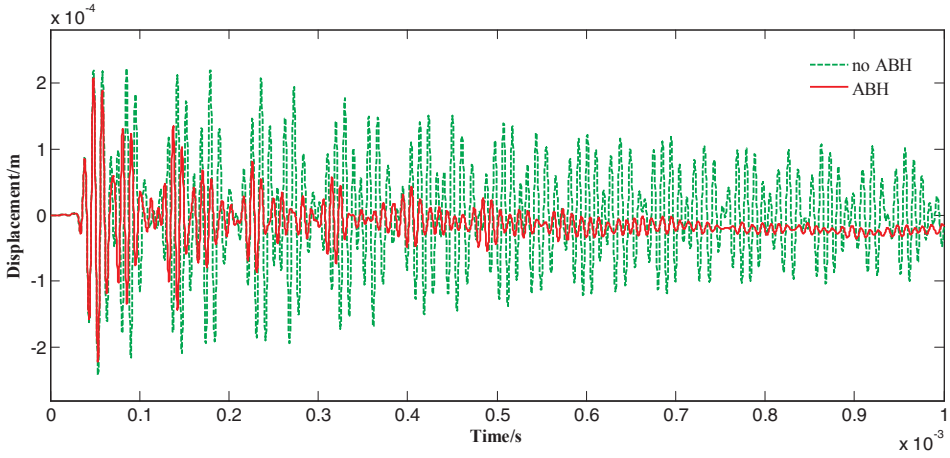

Fig. 9. The comparison of the output point displacement in the case (1).

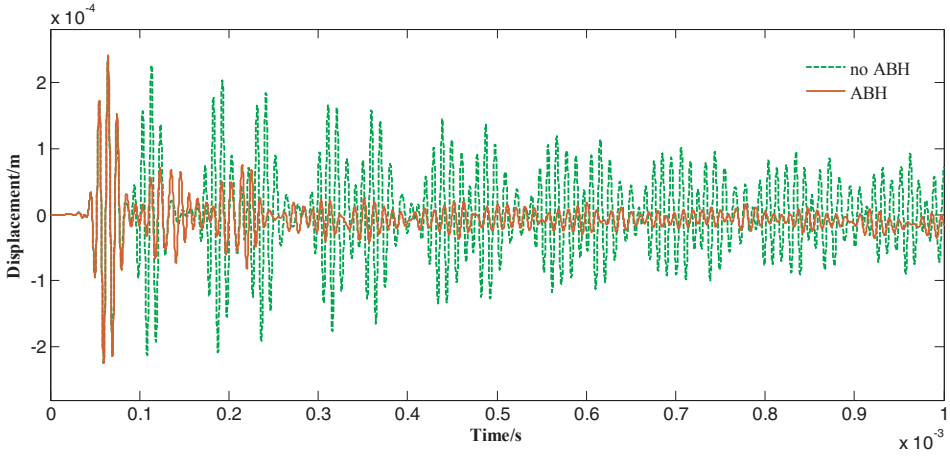

Fig. 10. The comparison of the output point displacement in the case (2).

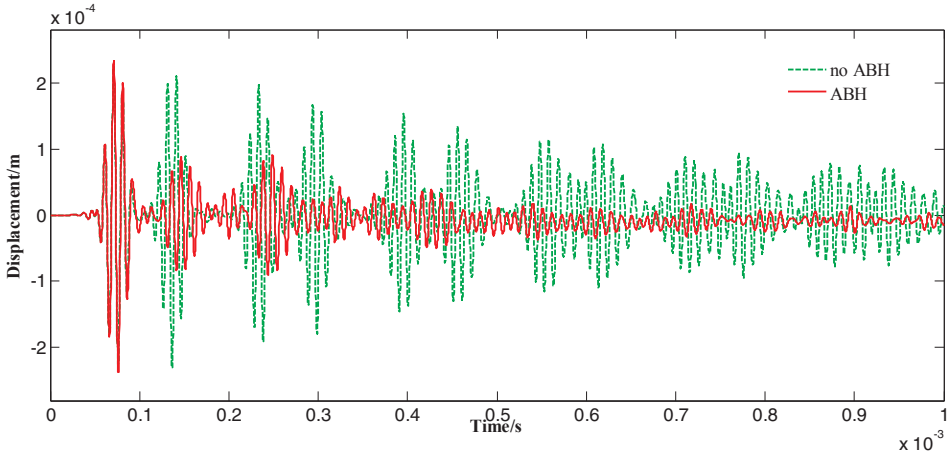

Fig. 11. The comparison of the output point displacement in the case (3).

$$\Delta t = \frac{l_{e\min}}{20 f_{\max}} \tag{6}$$

(2) Element size

In Ref. [33], it is recommended that more than ten nodes per wavelength are used, but a higher number is used in Refs. [32] and [34]. Thus the element length used in this study is

$$l_e = \frac{1}{20 k_{\max}} \tag{7}$$

with

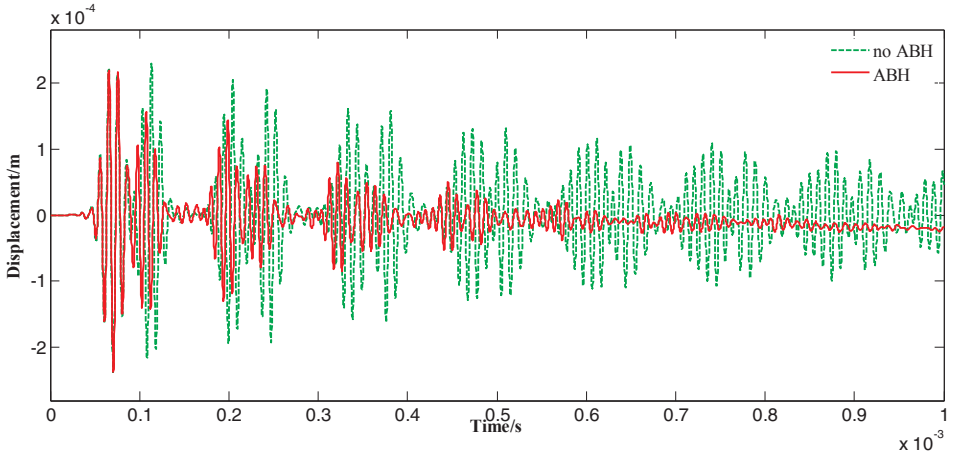

Fig. 12. The comparison of the output point displacement in the case (4).

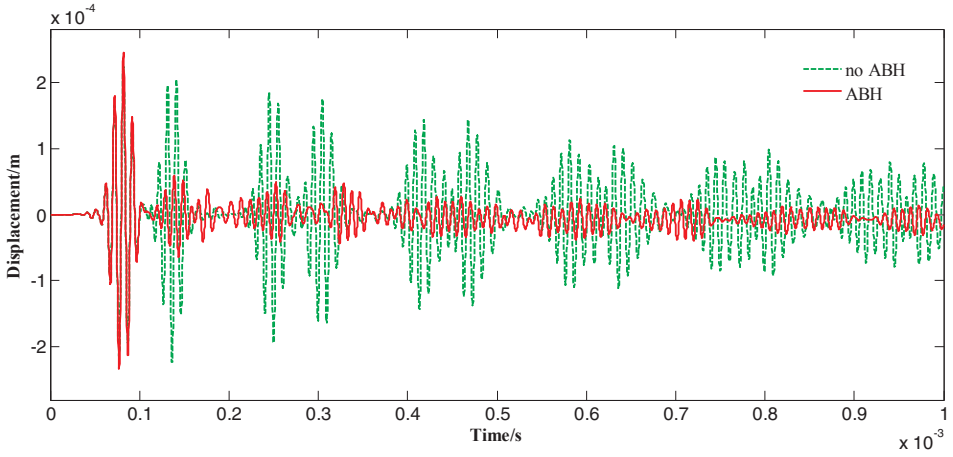

Fig. 13. The comparison of the output point displacement in the case (5).

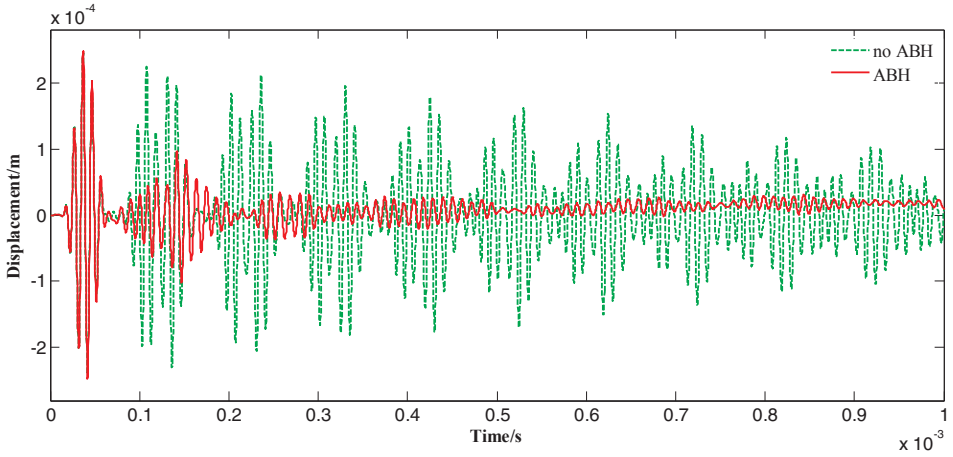

Fig. 14. The comparison of the output point displacement in the case (6).

$$k_{\max} = \frac{1}{\lambda_{\min}} \tag{8}$$

where $\lambda_{\min}$ is the shortest wavelength and $k_{\max}$ is the maximum wave number of interest. The shortest wavelength can be approximated by the transverse wave speed c_T and the maximum frequency is to be simulated. Hence the overall relation is

$$l_e = \frac{\lambda_{\min}}{20} \approx \frac{c_T}{20 f_{\max}} \tag{9}$$

In order to study the propagation characteristics of the AE wave in

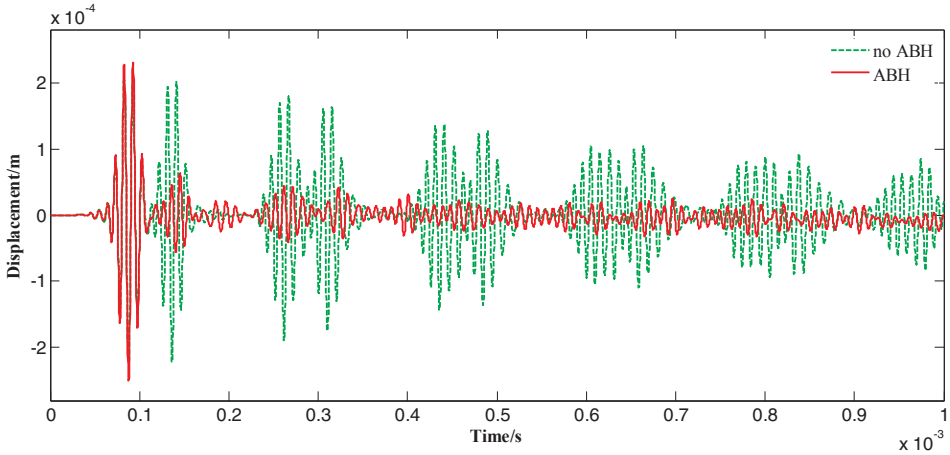

Fig. 15. The comparison of the output point displacement in the case (7).

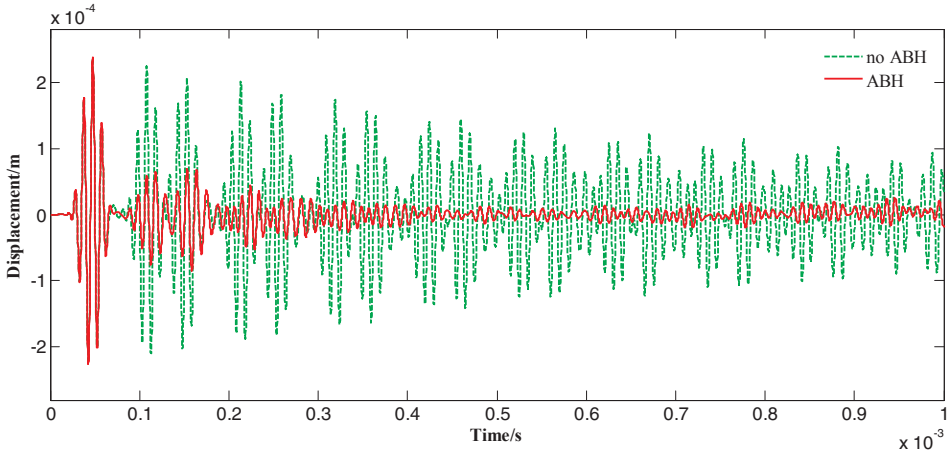

Fig. 16. The comparison of the output point displacement in the case (8).

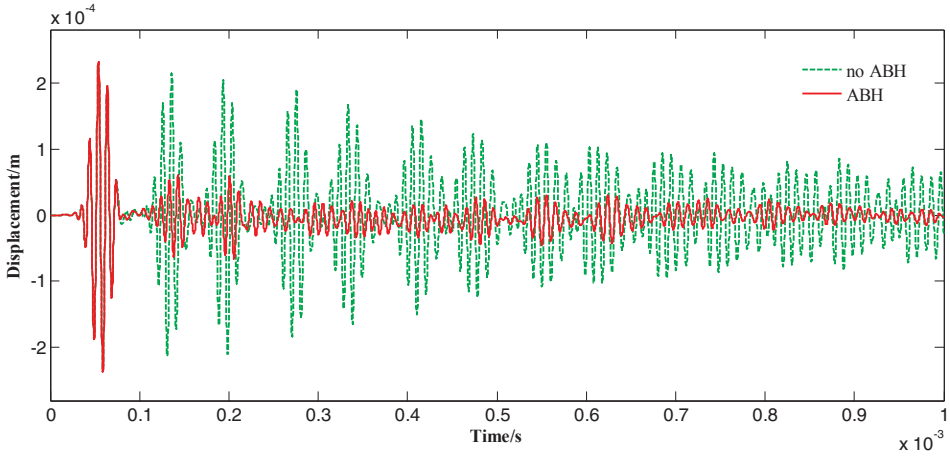

Fig. 17. The comparison of the output point displacement in the case (9).

the disc with the one-dimensional acoustic black hole structure, the disc model is established in the finite element software ABAQUS, as shown in Fig. 4.

In the laboratory environment, simulated AE signal excitation can be obtained by breaking lead on the surface of the structure. However, in the finite element simulation, the AE signal excitation can be obtained by loading step function. It is common to load one or several pairs of stepwise forces symmetrically on a cell node as a dipole source to represent a transient stimulus. As shown in Fig. 5, this paper uses a five-cycle burst tone excitation. The frequency of the AE wave is about 0.1 MHz. The excitation force size set in the established AE finite element simulation model is 1N. The disc is modeled by using C3D8R elements. At least twenty elements per local wavelength are used to guarantee the calculation accuracy. Material properties and

Table 4
Range analysis.

Test number	Factors				
	(a)	(b)	(c)	Empty column	Decrease ratio of energy (%)
(1)	1	1	1	1	77.92
(2)	1	2	2	2	78.62
(3)	1	3	3	3	70.08
(4)	2	1	2	3	66.58
(5)	2	2	3	1	73.98
(6)	2	3	1	2	81.05
(7)	3	1	3	2	73.57
(8)	3	2	1	3	84.07
(9)	3	3	2	1	79.37
T_{1j}	226.62	218.07	243.04	231.27	$T = \sum_{i=1}^{9} y_i = 685.24$
T_{2j}	221.61	236.67	224.57	233.24	
T_{3j}	237.01	230.50	217.63	220.73	
R_j	15.40	18.60	25.41	12.51	
Order of factors	(c)-(b)-(a)				
Best plan	$(a)_3(b)_2(c)_1$				

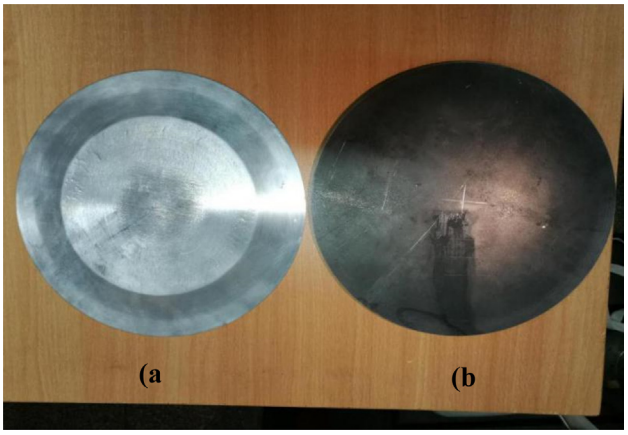

Fig. 18. The steel disc (a) with the acoustic black hole (b) without the acoustic black hole.

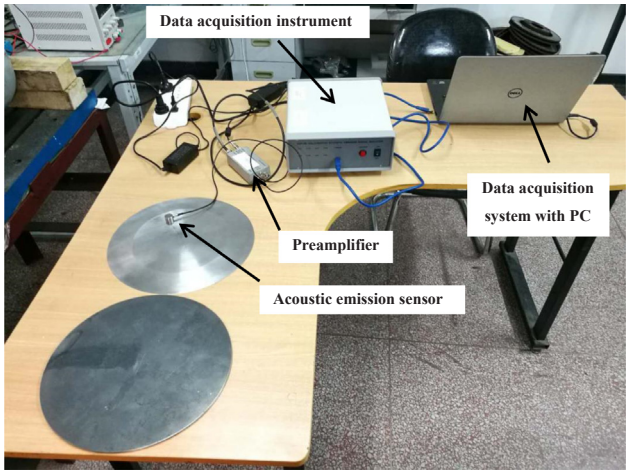

Fig. 19. Experimental setup of the AE detection.

geometrical parameters used in the finite element model are tabulated in Table 1.

According to the simulation method described above, the element size is 1 mm, which is enough to meet the accuracy requirements. And the time increment step is 0.01 us. The excitation is applied at the center of the upper surface of the disc and the simulation time is 0.3 ms. Figs. 6 and 7 show the simulated displacement cloud of the disc with and without the ABH, respectively.

By comparing displacement clouds, it can be found that the AE waves are concentrated by the ABH at the edge of the disc. In the disc without the ABH, most of the AE waves reach the edge of the disc and then reflect back to collect in the center of the disc. Simulation shows that the ABH can actually reduce reflected AE waves.

3. Parameter analysis and optimal combination

3.1. Parameter analysis

In order to study the influence of geometric parameters on the performance of the ABH, three influencing factors are selected, such as: (a) non-uniform thickness edge length a (mm), (b) distance of the measurement point (sensor) away from the edge of the upper surface b(mm), and (c) radius of the upper surface of the disc r_2 (mm). Using orthogonal test method to analyze the order of influence of these three factors, an orthogonal experiment of 3 factors and 3 levels are designed as shown in Table 2. Table 3 is the orthogonal test scheme.

As shown in Fig. 4, the disc with the ABH is of symmetry and periodicity. The plane of symmetry is modeled by using S4R elements (Fig. 8). Material properties and geometrical parameters used in the finite element model are listed in Table 1.

(1) The case with $a = 30mm,\ b = 20mm,\ r_2 = 100mm$.

Fig. 9 shows a comparison of the output displacement at point a (Fig. 8) of the structure with/without the ABH. The energy is expressed by the mean square value. The energy of the structure with/without the ABH is $6.2737 \times 10^{-6}\,m^2$ and $2.8410 \times 10^{-5}\,m^2$, respectively. The decay rates of energy is defined as

$$\frac{\text{Energy}_{\text{without the ABH}} - Energy_{\text{with the ABH}}}{\text{Energy}_{\text{without the ABH}}}$$

The decrease ratio of energy is 77.92%.

(2) The case with $a = 30mm,\ b = 40mm,\ r_2 = 150mm$.

Fig. 10 shows a comparison of the output displacement at point a (Fig. 8) of the structure with/without the ABH. The energy of the structure with/without the ABH is $4.5066 \times 10^{-6}\,m^2$ and $2.1083 \times 10^{-5}\,m^2$, respectively. The decrease ratio of energy is 78.62%.

(3) The case with $a = 30mm,\ b = 60mm,\ r_2 = 200mm$.

Fig. 11 shows a comparison of the output displacement at point a (Fig. 8) of the structure with/without the ABH. The energy of the structure with/without the ABH is $4.8962 \times 10^{-6}\,m^2$ and $1.6366 \times 10^{-5}\,m^2$, respectively. The decrease ratio of energy is 70.08%.

(4) The case with $a = 40mm,\ b = 20mm,\ r_2 = 150mm$.

Fig. 12 shows a comparison of the output displacement at point a (Fig. 8) of the structure with/without the ABH. The energy of the

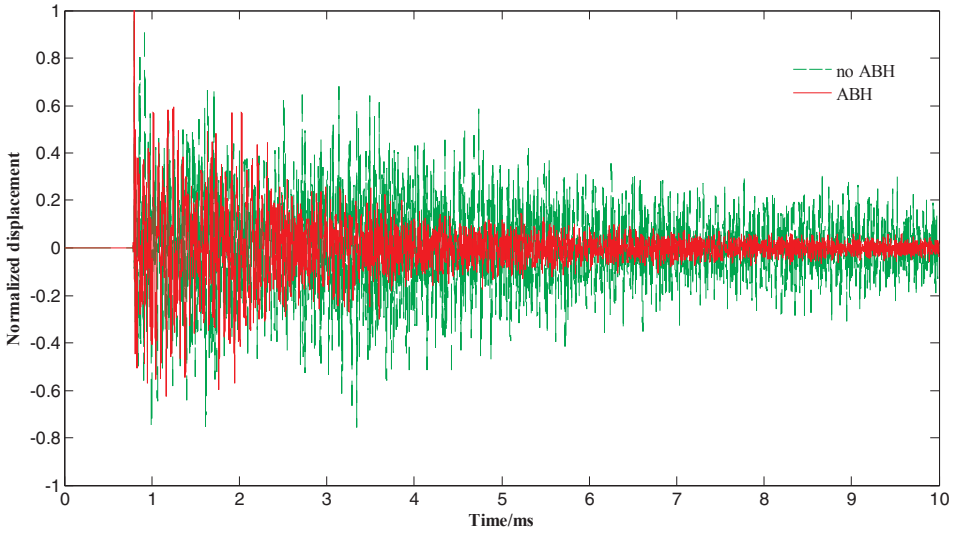

Fig. 20. The comparison of the signal received by the AE sensor at a distance of 20 mm from the upper surface of the disc with the ABH.

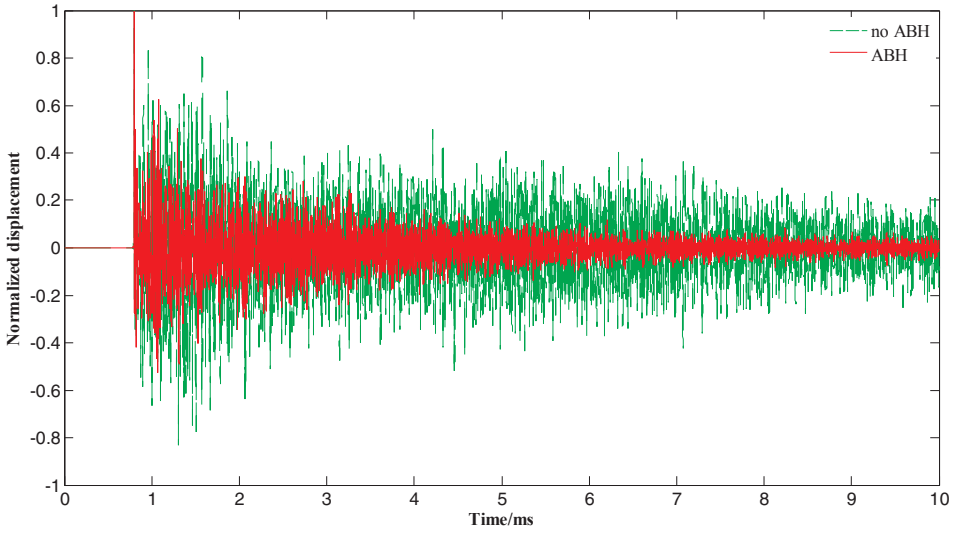

Fig. 21. The comparison of the signal received by the AE sensor at a distance of 40 mm from the upper surface of the disc with the ABH.

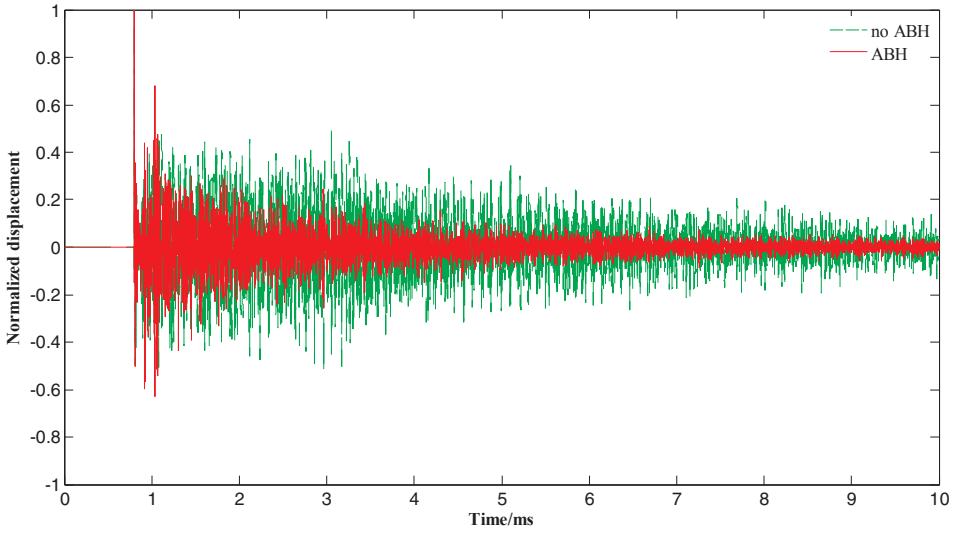

Fig. 22. The comparison of the signal received by the AE sensor at a distance of 60 mm from the upper surface of the disc with the ABH.

Table 5
The mean square value and decay rates of energy.

Cases		Mean square value	Decay rates of energy (%)
20 mm	With the ABH	1044.90	62.55
	Without the ABH	2790.20	
40 mm	With the ABH	570.06	76.61
	Without the ABH	2436.90	
60 mm	With the ABH	437.34	69.27
	Without the ABH	1423.2	

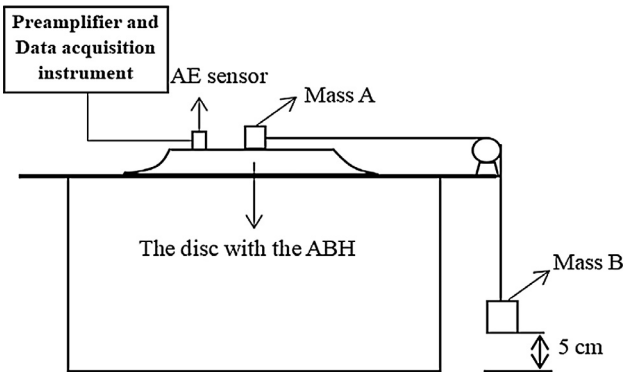

Fig. 23. Experimental setup of friction experiment. (a) Comparison of randomly extracted data. (b) Comparison of randomly extracted data.

structure with/without the ABH is $6.6036 \times 10^{-6}\,m^2$ and $1.9757 \times 10^{-5}\,m^2$, respectively. The decrease ratio of energy is 66.58%.

(5) The case with $a = 40mm,\ b = 40mm,\ r_2 = 200mm$.

Fig. 13 shows a comparison of the output displacement at point a (Fig. 8) of the structure with/without the ABH. The energy of the structure with/without the ABH is $4.1833 \times 10^{-6}\,m^2$ and $1.5692 \times 10^{-5}\,m^2$, respectively. The decrease ratio of energy is 73.98%.

(6) The case with $a = 40mm,\ b = 60mm,\ r_2 = 100mm$.

Fig. 14 shows a comparison of the output displacement at point a (Fig. 8) of the structure with/without the ABH. The energy of the structure with/without the ABH is $4.9131 \times 10^{-6}\,m^2$ and $2.5929 \times 10^{-5}\,m^2$, respectively. The decrease ratio of energy is 81.05%.

(7) The case with $a = 50mm,\ b = 20mm,\ r_2 = 200mm$

Fig. 15 shows a comparison of the output displacement at point a (Fig. 8) of the structure with/without the ABH. The energy of the structure with/without the ABH is $3.9538 \times 10^{-6}\,m^2$ and $1.4962 \times 10^{-5}\,m^2$, respectively. The decrease ratio of energy is 73.57%.

(8) The case with $a = 50mm,\ b = 40mm,\ r_2 = 100mm$

Fig. 16 shows a comparison of the output displacement at point a (Fig. 8) of the structure with/without the ABH. The energy of the structure with/without the ABH is $3.8452 \times 10^{-6}\,m^2$ and $2.4131 \times 10^{-5}\,m^2$, respectively. The decrease ratio of energy is 84.07%.

(9) The case with $a = 50mm,\ b = 60mm,\ r_2 = 150mm$

Fig. 17 shows a comparison of the output displacement at point a (Fig. 8) of the structure with/without the ABH. The energy of the structure with/without the ABH is $3.8924 \times 10^{-6}\,m^2$ and $1.8871 \times 10^{-5}\,m^2$, respectively. The decrease ratio of energy is 79.37%.

3.2. Optimal combination

Table 4 shows the range analysis of the calculation results, in which the results of each experimental level are added correspondingly to the i-th level of the j-th column. The sum is denoted as T_{ij}.

For better understanding, an example is described as follows. For the first column of Table 4, $T11 = y_1 + y_2 + y_3 = 77.92 + 78.62 + 70.08 = 226.62$, $T_{21} = y_4 + y_5 + y_6 = 66.58 + 73.98 + 81.05 = 221.61$, $T_{31} = y_7 + y_8 + y_9 = 73.57 + 84.07 + 79.37 = 237.01$. By comparing the sizes of T_{11}, T_{21}, and T_{31}, the general effect of factor (a) can be analyzed. R is defined as the range. $R_1 = \max\{T_{i1}\} - \min\{T_{i1}\} = T_{31} - T_{21} = 237.01–221.61 = 15.40$. The range of each column is not equal. It shows that the changes in the level of factors on the test results are not the same. The larger the range difference, the greater the effect of the change in the level of this factor on the test result. Through Table 4, we can get that $R_{(c)} > R_{(b)} > R_{(a)}$. The order of the primary and secondary effects of each factor is: (c) the radius of the upper surface of the disc, (b) distance of the sensor from the edge of the upper surface, and (a) non-uniform thickness edge length. The determination of the optimal solution involves choosing the optimal level for each factor. The level that maximizes each column should be chosen. Therefore, factor (a) level 3, factor (b) level 2 and factor (c) level 1 should be selected. The best plan is $(a)_3(b)_2(c)_1$.

4. Experimental verification

4.1. Broken-lead experiment

4.1.1. Experiment system

In order to verify the conclusion drawn in simulation above, the steel discs with/without ABH are processed for comparative experiments, respectively. Fig. 18(a) and (b) show the machined steel discs with/without ABH, respectively. The radius of the disc without the ABH is 150 mm. The radius of the upper surface and the lower surface of the disc with the ABH are 100 mm and 150 mm, respectively. The relation between the variation of the inhomogeneous thickness and the position is $h(x) = 0.00091461 \cdot x^{2.2}\ (0 \leqslant x \leqslant 50)$.

Fig. 19 shows the AE detection system. It includes an AE sensor which connected to the preamplifier to obtain the signal, and the data acquisition instrument which connected to the PC to analyze and process the signal. In order to compare with the simulation results, the AE sensors are placed at 20 mm, 40 mm and 60 mm away from the edge of the upper surface of the disc with the ABH, respectively.

Broken-lead experiment is a stable, reliable, and highly reproducible test method commonly used to simulate damage sources. Hsu [35] simulated the acoustic emission source by breaking the pencil lead in the direction of 30 degrees, and achieved good results. This method has been used as an acoustic emission analog source for calibrating acoustic emission sensors. The broken-lead experiments are done at the center of the upper surface of the disc with the ABH. Similarly, the same experiments on the disc without the ABH are performed. The sampling frequency in the experiment is 10 MHz and the sampling time is 0.01 s.

4.1.2. Experiment results

Figs. 20–22 show the comparison of the broken-lead signals received by the AE sensor at a distance of 20 mm, 40 mm and 60 mm away from the upper surface of the disc, respectively. For comparison, normalization is performed via the displacement divided by 2 times of the maximum amplitude of the direct wave. The mean square values that represent energy and decay rates of energy for the different cases are summarized in Table 5. The decay rates of energy are 62.55%, 76.61%, and 69.27%, respectively. From the energy decay rates, it can be seen that the experimental results are consistent with the simulation results qualitatively, but the effect of the test is not as good as the

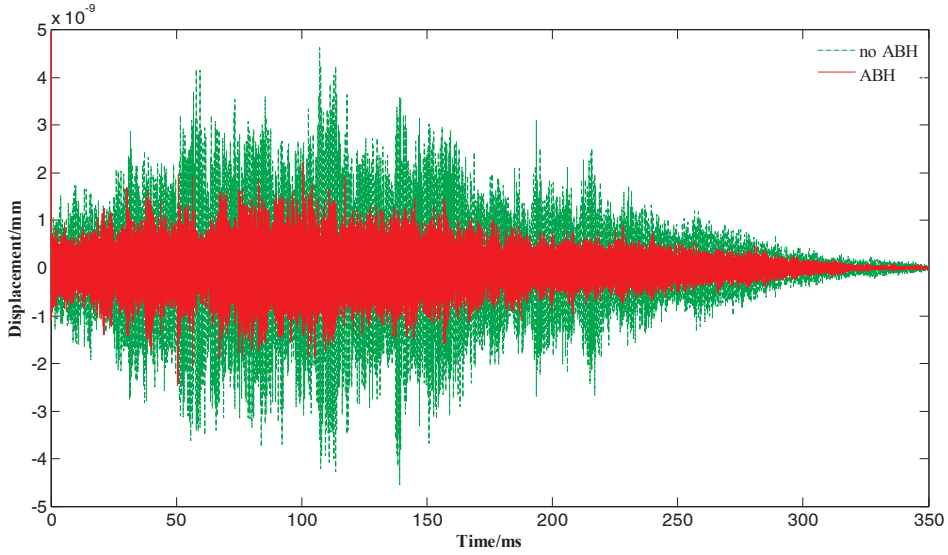

(a) Comparison of randomly extracted data.

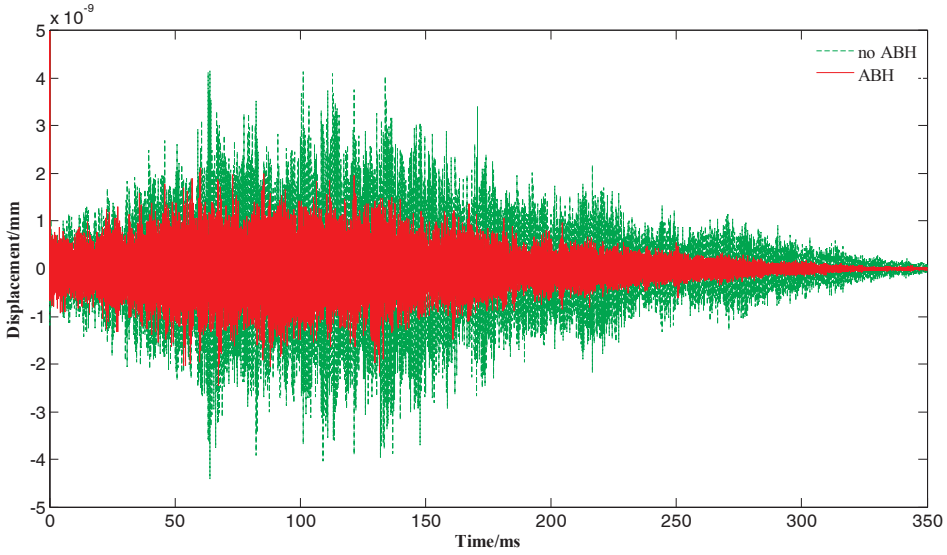

(b) Comparison of randomly extracted data.

Fig. 24. The comparison of the continuous friction experiments.

simulation. The reason is that the real ABH structure is limited by the manufacturing process and the ABH edge is difficult to let thickness equal to be zero in the form of high-order power function. Hence there exists the truncation at the edge of the disc, which obviously affects the energy aggregation effect of the ABH structure. A small truncation thickness can increase the reflection coefficient to 50–70% [24]. By using the improvement of processing technology, the effect would be better.

4.2. Friction experiment

As shown in Fig. 23, the friction experiment is performed to further verify the effect of the ABH to attenuate the reflected AE wave from the structure boundary. Mass A connected to mass B by an inelastic rope is placed in the middle of the disc for friction. Mass B falls freely at a height of certain 5 cm from the ground to produce friction. The AE sensor is placed 40 mm from the upper surface of the disc with the ABH. Similarly, the same experiment is done on the disc without the ABH. From the ABH experimental group and no ABH experimental group, 20 sets of data are collected respectively. As shown in Fig. 24(a) and (b), two sets of data are randomly taken for comparison. It is found that when the continuous friction AE signal propagates in the disc without the ABH, the displacement amplitude increases and becomes larger during the first 150 ms. This phenomenon is caused by the superposition of the reflected waves of the boundary with the direct waves. However, when the friction AE signal propagates in the disc with the ABH, the displacement amplitude is relatively stable during the first 150 ms. It shows that the reflected AE waves from the structure boundary are reduced. Then, the short-term frictional impact experiment is conducted. Such experiment is to apply a transient frictional shock on the disc to generate a burst-type acoustic emission signal. The signal data is normalized via the displacement divided by 2 times of the maximum amplitude of the direct wave, and the

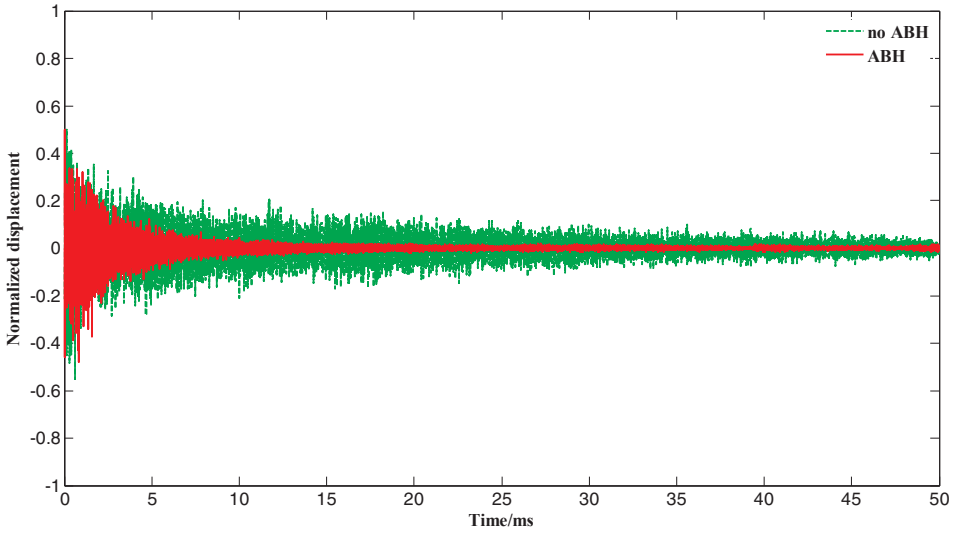

Fig. 25. The comparison of the short-term frictional impact experiments.

comparison of the results is shown in Fig. 25. By comparison, the decay rate of energy is 71.35%.

5. Conclusions

This paper introduces the ABH into a disc to attenuate AE reflection waves on the structure boundary before the sensor detects the AE reflection waves. Through simulation analysis, it is confirmed that the ABH can indeed reduce the reflected AE wave at the boundary. The othogonal test is conducted to reveal the influence of geometric parameters of the ABH on reflection attenuation. And a method based on the optimal parameter combination of the ABH is proposed to attenuate boundary reflection. The broken-lead and friction experiments are performed on the disc to verify the effect of the ABH to attenuate reflection of AE wave. Both analytical and experimental results show that the ABH is a candidate tool to reduce the AE reflection wave from the structure boundary, which could improve the accuracy of the acoustic emission tests.

Acknowledgement

This work was finically supported by the National Natural Science Foundation of China (Grant No. 51675023 & 51675021).

References

[1] G.C. McLaskey, S.D. Glaser, Mechanisms of sliding friction studied with an array of industrial conical piezoelectric sensors. Proc. SPIE 7647, Sensors and Smart Structures Technologies for Civil, Mechanical, and Aerospace Systems, 2010, p. 76471B.
[2] T. Kundu, S. Das, S.A. Martin, K.V. Jata, Locating point of impact in anisotropic fiber reinforced composite plates, Ultrasonics 48 (3) (2008) 193–201.
[3] T. He, D. Xiao, Q. Pan, et al., Analysis on accuracy improvement of rotor-stator rubbing localization based on acoustic emission beamforming method, Ultrasonics 54 (1) (2014) 318–329.
[4] T. Kundu, H. Nakatani, N. Takeda, Acoustic source localization in anisotropic plates, Ultrasonics 52 (6) (2012) 740–746.
[5] C.R. Heiple, S.H. Carpenter, Acoustic emission produced by deformation of metals and alloys-a review, J. Acoust. Emission 6 (1987) 177–204.
[6] E. Susič, I. Grabec, Application of a neural network to the estimation of surface roughness from AE signals generated by friction process, Int. J. Mach. Tools Manuf. 35 (8) (1995) 1077–1086.
[7] E. Govekar, E. Susi, P. Mu, et al., Self-organizing neural network application to technical process parameters estimation, Artif. Neural Networks 1 (1992) 579–582.
[8] H. Deresiewicz, Amontons and Coulomb, Friction's Founding Fathers. Approaches to Modeling of Friction and Wear, Springer, New York, NY, 1988, pp. 56–60.
[9] T.H. Heaton, Evidence for and implications of self-healing pulses of slip in earthquake rupture, Phys. Earth Planet. Interiors 64 (1) (1990) 1–20.
[10] L. Bureau, C. Caroli, T. Baumberger, Elasticity and onset of frictional dissipation at a non–sliding multi–contact interface, Proceedings of the Royal Society of London A: Mathematical, Physical and Engineering Sciences, The Royal Society, 2003, pp. 2787–2805.
[11] T. Kundu, Acoustic source localization, Ultrasonics 54 (1) (2014) 25–38.
[12] T. He, Y. Xie, Y. Shan, et al., Localizing two acoustic emission sources simultaneously using beam forming and singular value decomposition, Ultrasonics 85 (1) (2018) 3–22.
[13] S. Chen, E. Wang, Electromagnetic radiation signals of coal or rock denoising based on morphological filter, Proc. Eng. 26 (2011) 588–594.
[14] X.M. Chen, D.Z. Chen, Measuring average particle size for fluidized bed reactors by employing acoustic emission signals and neural networks, Chem. Eng. Technol. 31 (1) (2008) 95–102.
[15] M. Žvokelj, S. Zupan, I. Prebil, Non-linear multivariate and multiscale monitoring and signal denoising strategy using kernel principal component analysis combined with ensemble empirical mode decomposition method, Mech. Syst. Signal Process. 25 (7) (2011) 2631–2653.
[16] D. Mandic, N. Rehman, Z. Wu, et al., Empirical mode decomposition-based time-frequency analysis of multivariate signals: the power of adaptive data analysis, Signal Process. Mag., IEEE 30 (6) (2013) 74–86.
[17] N.E. Huang, Z. Shen, S.R. Long, A new view of nonlinear water waves: the Hilbert spectrum, Ann. Rev. Fluid Mech. 31 (1) (1999) 417–457.
[18] C. Zhou, Y. Zhang, Particle filter based noise removal method for acoustic emission signals, Mech. Syst. Signal Process. 28 (2012) 63–77.
[19] V.V. Krylov, A.L. Shuvalov, Propagation of localised flexural vibrations along plate edges described by a power law, Inst. Acoust. 22 (2000) 263–270.
[20] V.V. Krylov, F. Tilman, Acoustic 'black holes' for flexural waves as effective vibration dampers, J. Sound Vib. 274 (3–5) (2004) 605–619.
[21] V.B. Georgiev, J. Cuenca, F. Gautier, et al., Damping of structural vibrations in beams and elliptical plates using the acoustic black hole effect, J. Sound Vib. 330 (11) (2011) 2497–2508.
[22] S.C. Conlon, J.B. Fahnline, F. Semperlotti, Numerical analysis of the vibroacoustic properties of plates with embedded grids of acoustic black holes, J. Acoust. Soc. Am. 137 (1) (2015) 447–457.
[23] J.J. Bayod, experimental study of vibration damping in a modified elastic wedge of power-law profile, J. Vib. Acoust. 133 (6) (2011) 061003.
[24] E.P. Bowyer, D.J. O'Boy, V.V. Krylov, et al., Effect of geometrical and material imperfections on damping flexural vibrations in plates with attached wedges of power law profile, Appl. Acoust. 73 (5) (2012) 514–523.
[25] M.A. Mironov, Propagation of a flexural wave in a plate whose thickness decreases smoothly to zero in a finite interval, Sov. Phys. Acoust. – USSR 34 (3) (1988) 318–319.
[26] V. Denis, F. Gautier, A. Pelat, et al., Measurement and modelling of the reflection coefficient of an acoustic black hole termination, J. Sound Vib. 349 (2015) 67–79.
[27] V. Denis, A. Pelat, F. Gautier, et al., Modal overlap factor of a beam with an acoustic black hole termination, J. Sound Vib. 333 (12) (2014) 2475–2488.
[28] V.V. Krylov, Geometrical-acoustics approach to the description of localized vibrational modes of an elastic solid wedge, Sov. Phys. – Tech. Phys. 35 (2) (1990) 137–140.
[29] V.V. Krylov, Conditions for validity of the geometrical-acoustics approximation in application to waves in an acute-angle solid wedge, Sov. Phys. – Acoust. 35 (2) (1989) 176–180.

[30] J. Koreck, C. Valle, J. Qu, et al., Computational characterization of adhesive bond properties using guided waves in bonded plates, J. Nondestruct. Eval. 26 (2–4) (2007) 97–105.
[31] O.C. Zienkiewicz, R.L. Taylor, The Finite Element Method, Osborne McGraw-Hill, 2008.
[32] F. Moser, L.J. Jacobs, J. Qu, Modeling elastic wave propagation in waveguides with the finite element method, Ndt E Int. 32 (4) (1999) 225–234.
[33] D. Alleyne, P. Cawley, A two-dimensional Fourier transform method for the measurement of propagating multimode signals, J. Acoust. Soc. Am. 89 (3) (1991) 1159–1168.
[34] R. Seifried, L.J. Jacobs, J. Qu, Propagation of guided waves in adhesive bonded components, Ndt E Int. 35 (5) (2002) 317–328.
[35] N.N. Hsu, Acoustical birefringence and the use of ultrasonic waves for experimental stress analysis, Exp. Mech. 14 (5) (1974) 169–176.